Journal of Radioanalytical and Nuclear Chemistry
https://doi.org/10.1007/s10967-026-11143-0

A theoretical framework for isotope production at the SPES ISOL facility: Magnesium-28 as a case-study

G. S. Valli[1,2] · A. Arzenton[3,4] · A. Andrighetto[2] · D. Chen[3,4] · S. Corradetti[2] · A. Donzella[5,6] · O. S. Khwairakpam[2] · A. Leso[2,7] · S. Luise[3] · M. Lunardon[3,4] · S. Moretto[3,4] · D. Scarpa[2] · D. Serafini[2] · L. Zangrando[4] · E. Mariotti[1,8]

Received: 18 May 2026 / Accepted: 31 August 2026

Abstract
Isotope Separation On-Line (ISOL) is one of the techniques used for the production of exotic nuclides. This study presents a workflow for the theoretical modeling of the ISOL production of Mg-28. The production of isotopes in the target irradiated by protons, the diffusion and effusion processes leading to the release of the species from the target and the laser ionization of the atoms for the formation of the radioactive ion beam have been analyzed combining Monte Carlo simulations and theoretical models, in order to optimize the parameters of the system which most affect the production yield of the isotope.

Keywords ISOL · Mg-28 · GEANT4 · SPES_MED · Laser photo-ionization

Introduction

Developed in Copenhagen more than seventy years ago, the ISOL technique is adopted in many facilities to extract a pure isobaric and isotopic beam, that is lately collected on an adequate substrate or reaccelerated [1, 2]. In the ISOL technique, a primary beam of protons is accelerated towards a thick and hot target, causing several nuclear reactions. The produced atoms diffuse and effuse from the target material and eventually reach an ion source where they are ionized. The resulting ions are then electrostatically extracted and accelerated and separated by mass using suitable electromagnetic devices. Since the isotopes are generated at rest, the ISOL approach is particularly well suited for low-energy experiments and for post-acceleration using established techniques. Furthermore, it enables the production of radioactive isotopes for medical and other applications with very high purity and specific activity.

This technique is implemented at SPES (Selective Production of Exotic Species), a second-generation facility for Radioactive Ion Beam (RIB) production, currently in the advanced construction phase at the Legnaro National Laboratories of the Italian National Institute for Nuclear Physics (LNL-INFN). At SPES, RIBs are produced using a proton beam with an energy of approximately 40 MeV and a current of 200 μA, generated by a high-intensity cyclotron and directed onto a uranium carbide (UC_x), silicon carbide (SiC) or titanium carbide (TiC) target. With these values, neutron-rich radioactive isotopes can be created through uranium fission at a rate on the order of 10^{13} fissions per second [3]. Furthermore, radionuclidic purity levels ranging from 99.0 to 99.9% can typically be achieved using a low-resolution mass separation system. As a matter of fact, this system includes a Wien filter combined with a magnetic dipole and additional electrostatic elements that can improve the overall resolution up to about $\Delta M/M \approx 1/300$ [4]. Within the ISOL

✉ A. Arzenton
alberto.arzenton@pd.infn.it

1 Department of Physical Sciences, Earth and Environment, University of Siena, Via Roma 56, 53100 Siena, Italy

2 Legnaro National Laboratories, National Institute for Nuclear Physics, INFN-LNL, Viale dell'Università 2, 35020 Legnaro, Italy

3 Department of Physics and Astronomy, University of Padua, Via F. Marzolo 8, 35131 Padua, Italy

4 Padua Division, National Institute for Nuclear Physics, Via F. Marzolo 8, 35131 Padua, Italy

5 Department of Mechanical and Industrial Engineering, University of Brescia, Via Branze 38, 25123 Brescia, Italy

6 Pavia Division, National Institute for Nuclear Physics, Via A. Bassi 6, 27100 Pavia, Italy

7 Department of Physics and Earth Sciences, University of Ferrara, Via G. Saragat, 1, 44122 Ferrara, Italy

8 Pisa Division, National Institute for Nuclear Physics, Largo B. Pontecorvo 3, 56127 Pisa, Italy

Published online: 15 September 2026

framework at SPES, ion sources play a crucial role, as they enable the extraction of the exotic isotopes produced in the form of RIBs. Three kinds of sources are available [3]:

- Surface Ion Source (SIS), where ionization is caused by the contact with a hot surface;
- Plasma Ion Source (PIS), based on an electron plasma which indiscriminately ionizes all elements;
- Laser Ion Source (LIS), making use of resonant laser pulses.

Among these, the LIS is the most selective, as it exploits the quantum nature of atomic excitation [5, 6]. In simple terms, a set of laser beams with frequencies tuned to specific resonant transitions can progressively excite an outer electron, bringing it close to or beyond the ionization threshold through a step-wise population of excited states. Hence, if the laser bandwidth is sufficiently narrow, only the desired element is ionized. Moreover, in some cases, extremely narrow bandwidths also allow the exploitation of hyperfine structure to distinguish between isotopes, although this high level of selectivity can be reduced by Doppler and other broadening effects. The design, mechanical structure, thermal behavior, and performance of the SPES LIS have been described in the literature [7, 8].

In this context, SPES_MED is a three-year project funded by CSN3 of INFN and focused on the SPES facility. It brings together interdisciplinary efforts from the LARAMED (LAboratory of RAdionuclides for MEDicine) and ISOLPHARM (ISOL technique for radioPHARMmaceuticals) projects. Its main goals are to measure nuclear cross sections in order to optimize the production of medical radionuclides, to determine ISOL production yields from SiC and TiC targets, and to compare experimental results with existing simulation libraries to provide reliable benchmarks when theoretical predictions are inadequate.

The present work is carried out within the SPES_MED framework and focuses on the development of a workflow for the theoretical and computational modeling of ISOL radionuclide production, simulating both diffusion and effusion processes as well as laser photo-ionization in a comprehensive time-resolved model. Mg-28, an important radiotracer with applications in biology, is used as a case study [9, 10].

Starting from the work by Kirchner in 1992 [11], which introduced the formalism for the release in ion-catcher systems, several Monte Carlo codes were developed to simulate the release of short-lived species from ISOL targets [12–14]. For example, the release time can be estimated with designed codes such as RIBO [12] and Diffuse II [14]. Although such codes proved to be reliable and able to replicate experimental data under specific conditions, they cannot be adapted to specific setups without the interaction with the developers, and are consequently unlikely to be used to simulate various target configurations.

In this work, the GEANT4 Monte Carlo toolkit was used to simulate both the production of atoms and their release mechanisms [15]. The latter are theoretically explained in the next Section. The main advantage of the GEANT4 code is its flexibility, which allows extensive customization according to the specific requirements of the user.

The first objective is to estimate the average number of radionuclides produced by fission within the SPES SiC target and to evaluate the mean release time, comparing it with the isotope half-life. The second part of the study is devoted to the resonant laser photo-ionization of magnesium. Two different two-step excitation schemes are analyzed and compared: one identified within the ISOLPHARM project, suitable for lasers at SPES, and another reported in the literature, previously investigated at ISOLDE/CERN [16, 17]. Finally, an estimate of single-pulse and overall ionization efficiency is presented.

Theory

In general, the overall yield of the process can be expressed by the following formula [18]:

$$Y = \sigma \Phi N \varepsilon_d \varepsilon_e \varepsilon_i \varepsilon_t. \quad (1)$$

The term $R = \sigma \Phi N$ represents the in-target production rate of the nuclides of interest. In this expression, σ identifies the nuclear cross section for the desired reaction, Φ is the proton beam flux and N is referred to the number of nuclei of the species present in the target. The efficiency coefficients ε_d and ε_e account for delays and radionuclide losses occurring during diffusion and effusion processes within the target, respectively. These factors reflect the fact that a fraction of the produced nuclei may decay during these time intervals, become trapped on surfaces, or otherwise be lost from the system. The product of ε_d and ε_e is often referred as release efficiency ε_r. The efficiency factor ε_i represents the ionization process. Finally, ε_t is the efficiency coefficient that summarizes the beam purification and transport processes and depends on the beam line length and device quality. However, a time-resolved model could facilitate the understanding and the optimization of several constructive or physical parameters of the system: this is the reason behind the following theoretical analysis.

After the nuclear reactions induced by the proton beam striking the target, the release of the produced radioisotope is governed by two successive processes that can, to a good approximation, be treated as independent: diffusion and effusion. The whole process is illustrated in Fig. 1. Diffusion is the process by which radioisotopes are transported

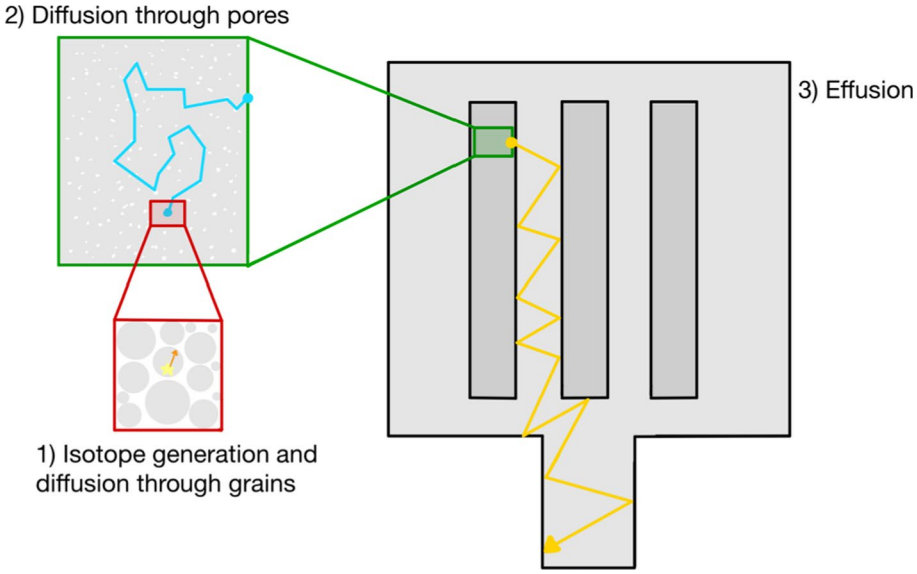

Fig. 1 Scheme of the release processes: diffusion and effusion

within the target as a result of random molecular motions. The target consists of seven disks contained within a vacuum chamber, as detailed in the next section. Considering the reasonable assumption of spherical target material grains/molecules, the average time $\langle t_{diff} \rangle$ spent by a particle to exit the grain/molecule can be calculated solving exactly the second Fick's Law for a perfect sphere [19], which leads to:

$$\langle t_{diff_s} \rangle = \frac{a^2}{15D}, \tag{2}$$

where a is the radius of the sphere and D is the diffusion coefficient. This latter depends on the temperature T of the material and is regulated by the Arrhenius equation:

$$D(T) = D_0 \exp\left(\frac{E_a}{k_B T}\right), \tag{3}$$

where D_0 is the diffusion coefficient when the temperature diverges to infinity, k_B is the Boltzmann coefficient and E_a is the activation energy, namely the energy required by an atom to move from a site to another [20]. As the nuclide leaves the grain/molecule, the diffusion through the target material pores is initiated. In such a case, the random walk can be modeled as an isotropic diffusive process, of the order of magnitude of the average pore size. Therefore, the mean free path for porous diffusion is: $MFP = 2D_p/v$, where D_p is the porous diffusion coefficient and $v = 1/\langle t_{diff_p} \rangle$.

After the nuclide reaches the target surface, it can be desorbed and travels freely in the target box until it reaches another solid surface. During the effusion process there are many collisions in the target container before the radionuclide reaches the ion source. At every collision the nuclide can be adsorbed by a surface it collides with with a certain probability, which can be estimated with dedicated tests involving the target assembly materials [21]. To continue to the ion source, the nuclide needs to be desorbed by the surface, affecting the probability of decaying inside the target container. The average delay between an adsorption and the consecutive desorption is referred to as "sticking-time". Various distributions can be used to model the random exiting angle of a particle from a surface. For example, the Lambertian distribution describes the reflection of atoms in vacuum systems [12]. The total effusion time can be estimated with:

$$\tau_{eff} = \chi\left(\tau_{free} + \tau_{stick}\right), \tag{4}$$

where χ is the mean number of collisions of the atom with chamber surfaces. The sum $\tau_{free} + \tau_{stick}$ represents the average time between two collisions, determined by the mean free flight time τ_{free} and the mean sticking time τ_{stick}, which depends on the type of diffusing nuclide and on the material that absorbs it. The sticking time depends on the temperature and on the enthalpy of adsorption of the surface, according to the law defined by Frenkel [20]:

$$\tau_{stick} = \tau_0 \exp\left(-\frac{E_d}{RT}\right), \tag{5}$$

where E_d is the interaction energy between the adsorbed atom and the surface, approximately equal to the molar enthalpy of absorption of the surface, R is the gas constant, and T is the surface temperature. Hence the total mean release time from the target is:

$$\langle t \rangle = \langle t_{diff_s} \rangle + \langle t_{diff_p} \rangle + \langle t_{eff} \rangle. \tag{6}$$

Considering all the processes that can occur within the target, namely isotope production, release and decay, the

differential equation that describes the temporal variation in the number of desired atoms N present in the cavity is:

$$\dot{N}_{\text{target}}(t) = R - \lambda N(t) - kN(t) \tag{7}$$

where R is the isotope production rate, λ is the isotope decay constant and $k = \langle t \rangle^{-1}$. Assuming that $N(0) = 0$, the solution of Eq. (7) results:

$$N_{\text{target}}(t) = \frac{R}{k+\lambda}\left(1 - e^{(-(k+\lambda)t)}\right), \tag{8}$$

from which it is possible to calculate the flow of atoms that, after being released, enter.

the ion source:

$$\Phi_{in}(t) = kN_{\text{target}}(t). \tag{9}$$

The LIS exploits photo-ionization of the atoms: laser beams tuned to specific resonant transitions are able to push the most external electron close to the ionization threshold, or even over it, via stepwise population of a few excited states of the atoms of interest. Such a system can be described by the quantum density matrix, whose diagonal elements represent the atomic populations, while the off-diagonal elements are called "quantum coherences" [22]. For the case of Mg, two different two-step photo-ionization schemes were considered:

1. $2p^6 3s^2\ {}^1S_0 \rightarrow 3s3p^1P_1^0 \rightarrow 3s3d^1S_2$;
2. $2p^6 3s^2\ {}^1S_0 \rightarrow 3s3p^1P_1^o \rightarrow 3s4d^1D_2$.

Scheme 1 was identified within the ISOLPHARM project and Scheme 2 was investigated at ISOLDE/CERN [16, 17].

The schemes start from the ground state and are characterized by two resonant steps: the first one is common to both of them, with a corresponding wavelength $\lambda_1 = 285.21$ nm; the second step is different, with $\lambda_2 = 880.68$ nm for Scheme 1, reproducible with SPES lasers [7], and $\lambda_2' = 552.84$ nm for Scheme 2. Regarding the decay modes, in Scheme 1 the first excited state decays directly to the ground state, while the second excited state decays either to the ground state or to the first excited state. Scheme 2 is similar to Scheme 1, except for the fact that the second excited state doesn't decay to the ground state. Both schemes are represented in Fig. 2, where a third green laser with $\lambda_3 = 532$ nm is used for non-resonant ionization. Hence, four populations are considered: ground state, 1st excited level, 2nd excited level and ion state. The equations describing their time derivatives and the time derivatives of quantum coherences, respectively, for Scheme 1 are given as:

$$\begin{aligned}\dot{\rho}_{11}(t) = &-\frac{i}{2}\Omega_{21}(t)\,\rho_{12}(t) + \frac{i}{2}\Omega_{12}(t)\,\rho_{21}(t)\\ &+ 2\big(A_{21}\,\rho_{22}(t) + A_{31}\,\rho_{33}(t)\big);\end{aligned} \tag{10}$$

$$\begin{aligned}\dot{\rho}_{22}(t) = &-\frac{i}{2}\Omega_{12}(t)\,\rho_{21}(t) + \frac{i}{2}\Omega_{21}(t)\,\rho_{12}(t) - \frac{i}{2}\Omega_{32}(t)\,\rho_{23}(t)\\ &+ \frac{i}{2}\Omega_{23}(t)\,\rho_{32}(t) + 2A_{32}\,\rho_{33}(t) - 2A_{21}\,\rho_{22}(t);\end{aligned} \tag{11}$$

$$\begin{aligned}\dot{\rho}_{33}(t) = &-\frac{i}{2}\Omega_{23}(t)\,\rho_{32}(t) + \frac{i}{2}\Omega_{32}(t)\,\rho_{23}(t)\\ &- 2\big(A_{32} + A_{31} + \gamma_i(t)\big)\rho_{33}(t);\end{aligned} \tag{12}$$

$$\dot{\rho}_{ion}(t) = 2\,\gamma_i(t)\,\rho_{33}(t); \tag{13}$$

$$\begin{aligned}\dot{\rho}_{12}(t) = &\frac{i}{2}\Omega_{12}(t)\big[\rho_{22}(t) - \rho_{11}(t)\big] - \frac{i}{2}\Omega_{32}(t)\,\rho_{13}(t)\\ &- \big(A_{32} + A_{31} + 2\gamma_{L1}\big)\rho_{12}(t);\end{aligned} \tag{14}$$

$$\begin{aligned}\dot{\rho}_{23}(t) = &\frac{i}{2}\Omega_{23}(t)\big(\rho_{33}(t) - \rho_{22}(t)\big) - \frac{i}{2}\Omega_{21}(t)\rho_{13}(t)\\ &- \big(A_{32} + A_{31} + \gamma_i(t) + 2\gamma_{L2}\big)\rho_{23}(t);\end{aligned} \tag{15}$$

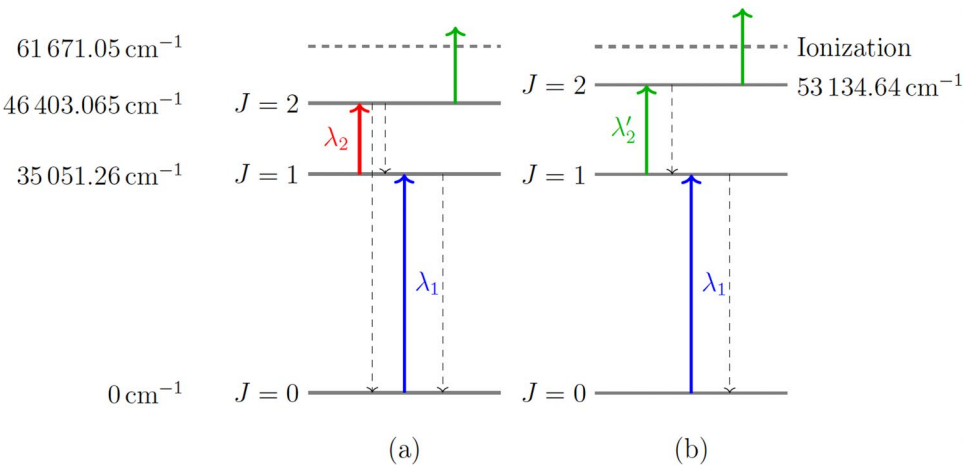

Fig. 2 Two-step laser ionization schemes for Mg

$$\dot{\rho}_{13}(t) = \frac{i}{2}\Omega_{12}\rho_{23} - \frac{i}{2}\Omega_{23}\rho_{12} - \left(A_{32} + A_{31} + \gamma_i(t) + 2\gamma_{L1} + 2\gamma_{L2}\right)\rho_{13}, \quad (16)$$

where A_{ij} is the Einstein A-value of the $i \rightarrow j$ transition, representing the decay rate, Ω_{ij} is its Rabi frequency, expressing the oscillation frequency of the probability amplitudes of the two states, $\gamma_i(t)$ is the non-resonant ionization rate and γ_{Li} is the Lorentzian bandwidth of the i-th laser. The solution of Eq. (13), combined with η, expressing the ratio between the laser interaction volume and the LIS volume, gives the single-pulse ionization efficiency of the photon-atom interaction. Theoretical details on the model parameters can be found in literature [23]. It is important to notice that, if the resulting efficiency is related to the physical interactions within one pulse of the lasers, to obtain the overall efficiency of the LIS, this value has to be integrated in time, together with the pulse rate, the atom flux from the target, the loss rate implied by the thermal–mechanical properties of the system and the radioactive decay. A simple differential equation considering the atom flux Φ_{in}, the single-pulse photo-ionization efficiency $\varepsilon_{i_{sp}}$, the radioactive decay constant λ and a loss factor l can express the amount of the non-ionized nuclide of interest in the LIS [23]:

$$\dot{N}_{LIS}(t) = \Phi_{in} - \varepsilon_{i_{sp}} r N(t) - l N(t) - \lambda N(t), \quad (17)$$

whose solution for $N(0) = 0$ is:

$$N_{LIS}(t) = \frac{\Phi_{in}}{\varepsilon_{i_{sp}} r + l + \kappa}\left[1 - e^{-\left(\varepsilon_{i_{sp}} r + l + \kappa\right)t}\right]. \quad (18)$$

The ion flux exiting the ion source is then:

$$\Phi_{out}(t) = \varepsilon_{i_{sp}} r N(t). \quad (19)$$

Finally, the time evolution of the nuclide population accumulated on the collection target, $N_{coll}(t)$, can be modeled through a dynamic balance between the ion flux extracted from the LIS source, $\Phi_{out}(t)$, and the spontaneous decay rate of the radionuclide. The fundamental differential equation is given by:

$$\dot{N}_{coll}(t) = \Phi_{out}(t) - \lambda N_{coll}(t) \quad (20)$$

By substituting Eq. (19) to $\Phi_{out}(t)$ and applying the initial condition $N_{coll}(0) = 0$, solving the differential equation yields $N_{coll}(t)$. Multiplying this solution by the decay constant λ provides the final analytical equation for the collected activity:

$$A_{coll}(t) = \Phi_{out,ss}\left[1 - e^{-\lambda t} + \frac{\lambda}{\lambda - \gamma}\left(e^{-\lambda t} - e^{-\gamma t}\right)\right], \quad (21)$$

where $\Phi_{out,ss}$ is the stationary solution of Eq. 19 and $\gamma = \varepsilon_{i_{sp}} r + l + \kappa$.

The key concept of the time-resolved model is expressed by Eqs. (7) and (17); it can offer a deeper perspective with respect to the standard one, expressed by Eq. (1) [15, 18], and pave the way for a better investigation of not well-known effects in ISOL facilities. In this work, it is applied to the LIS, but a customization of Eq. (17) could adapt it also to SIS and PIS.

Computational methods

Geant4 simulations

The estimation of the production rate in the target and the release efficiency can be performed using the GEANT4 Monte Carlo toolkit. It allows for the simulation of the passage of particles through matter and provides a wide set of libraries, which can be employed from simple single studies of basic phenomena to full-scale detector simulations [24–26]. In particular, the ISOLPHARM project developed the open source G4_ISOL_RELEASE application [15]. This code is computing intensive; thus, it is executed thanks to the support of a Cloud infrastructure in the CloudVeneto [27], which allows to launch 10^{10} events, guaranteeing an uncertainty < 3%.

The simulated apparatus, shown in Fig. 3, includes all components of the target block assembly, namely seven SiC disks, a tantalum (Ta) container and a transfer line, as well as a graphite (C) enclosure with its windows and beam dumps.

The values of the density of the target material (ρ = 3.04 g/cm^3), of the radius of the grains (between 4 and 10 μm) and of the radius of the porous (r_{porous} = 50 μm)

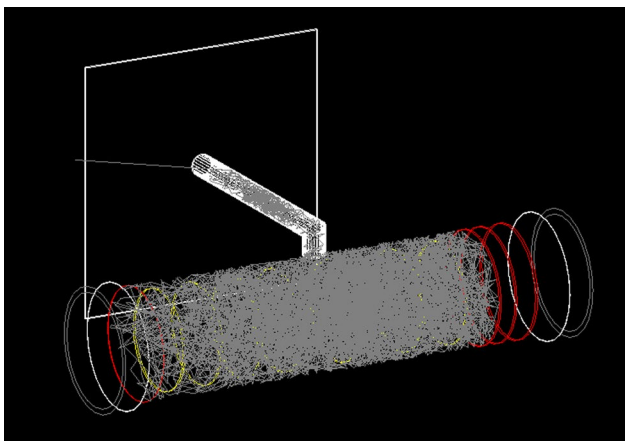

Fig. 3 Implemented geometry in GEANT4. Color code: yellow = SiC, red = C, white = Ta, gray = trajectory of one Mg-28 atom

Table 1 Thickness values of the target disks in millimeters

	Disk 1	Disk 2	Disk 3	Disk 4	Disk 5	Disk 6	Disk 7
Small t	1.0	0.9	0.9	0.8	0.7	0.6	0.5
Big t	0.8	0.8	0.8	0.8	0.8	0.8	0.8

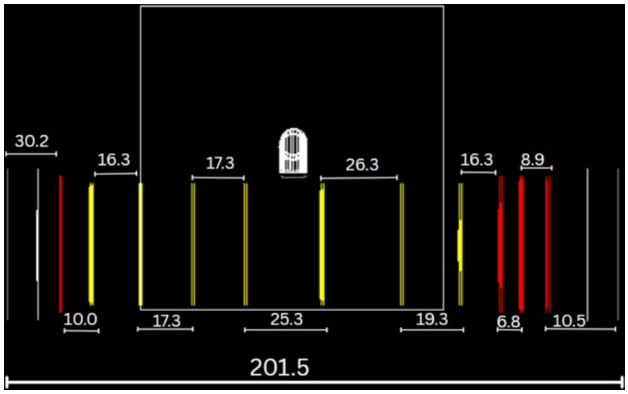

Fig. 4 Side view of the small target. The SiC disks are shown in yellow, the graphite enclosure in red, and the tantalum components (container and transfer line) in white. All distances are given in millimeters

were taken from literature [28]. The type of silicon carbide considered is SiC SP. The simulation of isotope production is performed using two different target geometries irradiated with a 40 MeV proton beam at a current of 200 µA, with each event representing a proton of the beam hitting the target. Since one configuration features smaller disks placed closer together than the other, the two setups are referred to as the "small target" and the "big target". This comparison was carried out to evaluate which geometry provides higher isotope release efficiency, alongside other simulation parameters such as temperature and target composition. In the small target, the diameter of the target disks is 13 mm, the thickness in millimeters of the disks is reported in Table 1 and distances in millimiters between disk centers are shown in Fig. 4. The big model, instead, uses 0.8 mm thick disks with 20 mm diameter.

The simulation diffusion processes consist of two stages: diffusion of the radionuclide within the target material grains, governed by the diffusion coefficient, and a secondary diffusion through the pores, described by a porous diffusion coefficient. Based on the grain size distribution of the target material, the code randomly generates an average escape time for each nuclide using Eq. (2). Grain radii are generated using a Gaussian distribution, with the mean set to the midpoint of the literature range (4–10 µm) [28] and the standard deviation chosen so that 99.7% of values fall within this interval. The code requires the diffusion coefficient, which has been calculated using Eq. (3), based on temperature, activation energy, and a

Table 2 Input parameters for diffusion

T	$\langle a \rangle$	σ_a	D_0	E_a
2273 K	7 µm	1 µm	0.0249 cm^2/s	92.24 kcal/mol

pre-exponential factor D_0 derived from literature data for magnesium diffusion in SiC [29], whose value is reported in Table 2.

Once the nuclide reaches the grain surface, diffusion through the pores begins. Due to the lack of literature data for the porous diffusion coefficient of magnesium in SiC, D_p was studied in the range from $D_p = 10^2$ cm^2/s and $D_p = 10^{12}$ cm^2/s, with the endpoints being referred to as "slow" and "fast" release conditions. In terms of orders of magnitude, this choice maintained the same difference between D and D_p as in the reference [15]. These coefficients are also treated using the Arrhenius law, in order to estimate $D_{0,p}$.

The emission of particles from the surface is modeled using a Lambertian angular distribution to determine the emission direction, while their kinetic energy is sampled from a Maxwell–Boltzmann distribution. During the effusion process, there is in principle a probability that nuclides are reabsorbed and diffuse back into the target disks; however, in the simulation this probability is set to zero. Instead, reabsorption is considered in the components of the target container: particles are re-emitted after a mean sticking time, which is added to the total escape time. Nevertheless, if the total time exceeds 100 h, the isotope is killed by the simulation [15]. As limited data are available in literature regarding the sticking times of magnesium on tantalum, a value was derived using the "Eichler systematics" [20, 30–32], an empirical model that provides approximate estimates of adsorption enthalpies on metallic surfaces. The obtained value in [20] refers to a temperature of 2400 °C, which is significantly higher than the actual simulation temperature of the target (≤ 2000 °C). In the absence of more accurate data, this leads to an estimated mean sticking time of $\tau_{stick,Ta} \approx 5{\times}10^5$ ns. For graphite, experimental data are available for the sticking times of some alkali metals in the temperature range 1400–1700 K [33]. Since no data are available for magnesium, sodium was used as a proxy, being the closest element in atomic mass among those studied. From the fit of the experimental data, the mean sticking time at the temperature of interest was estimated as $\tau_{stick,C} \approx 1.94{\times}10^4$ ns.

Table 3 Laser photo-ionization parameters for Mg

Parameter	Value	Source
λ_1	285.21 nm	[35]
λ_2	880.67 nm	[35]
λ_2'	552.84 nm	[16]
ρ_{laser}	1.55 mm	[36]
τ_{FWHM}	30 ns	[7]
T	$3 \cdot \tau_{FWHM}$	[23]
A_{21}	$4.91 \cdot 10^8\ s^{-1}$	[34]
A_{32}(Scheme 1)	$1.27 \cdot 10^7\ s^{-1}$	[34]
A_{32}(Scheme 2)	$1.39 \cdot 10^7\ s^{-1}$	[34]
A_{31}	$1.64 \cdot 10^3\ s^{-1}$	[34]
γ_{Li}	6 GHz	[7]
σ	$10^{-18}\ cm^2$	[23]
r	10 kHz	[6, 37]

Laser photo-ionization model parameters

Laser photo-ionization is studied using the density matrix. The solution of Eq. (13) gives the value of the ion yield, which, multiplied by the volume factor η, is the single-pulse ionization efficiency. The parameters considered in this study, chosen to reproduce the SPES online configuration, are summed up in Table 3. In particular, τ_{FWHM} and T denote the Full Width at Half Maximum (FWHM) of the Gaussian laser pulse and its overall duration, respectively. The parameter ρ_{laser} corresponds to the laser spot radius, chosen to maximize the interaction volume within the LIS. The Rabi frequencies for all allowed transitions are computed using Wigner coefficients and subsequently averaged, while the Einstein coefficients are obtained from a computational database [34]. The order of magnitude of σ, the cross section of the process, is selected based on the practical limitation that commercially available lasers are generally tunable to saturate non-resonant transitions [23]. The parameter T is chosen to ensure that the contributions from the tails of the Lorentzian and Gaussian distributions are not neglected. Finally, the photo-ionization of Mg is analyzed by varying the average laser powers.

Results and discussion

Release processes

The production of Mg-28 was investigated using a 40 MeV, 200 µA proton beam. The dominant reaction channel is expected to be Si-30(p, 3p)Mg-28, proceeding via compound nucleus formation followed by proton evaporation. According to GEANT4 simulations, the predicted production rates are $8.2 \cdot 10^{-8}$ atoms per proton for the small target and $6.4 \cdot 10^{-8}$ atoms per proton for the big target, as expected from disk thickness (Table 1). Mg-28 disk distribution is also a useful information: the atoms are produced exclusively in the first two disks, see for example Fig. 5, where 91.46% of the isotopes is generated in the first disk. Considering the maximum proton current achievable experimentally, namely 200 µA, it is possible to estimate the maximum number of Mg-28 atoms produced per second, equal to $1.02 \cdot 10^8$ atoms/s with a percentage error of 3% in the small target and, in the big one, $8.00 \cdot 10^7$ atoms/s with a percentage error of 2%. In comparison, FLUKA-based simulations [38] in the literature report a production rate of $8.75 \cdot 10^6$ atoms/s in the big target, accompanied by a significantly higher uncertainty of 40% [39]. The approximately one-order-of-magnitude discrepancy between these results can be primarily attributed to differences in the underlying nuclear cross-section models and reaction libraries utilized by FLUKA compared to those adopted in the present work. Furthermore, the lower percentage error obtained in this study highlights a higher statistical precision, though direct experimental validation upon the commissioning of SPES will be fundamental to benchmark these models.

For both target geometries, the diffusion and effusion processes of Mg-28 are simulated considering only the first two disks, as these are the regions where the production of the isotope of interest is concentrated. The escape time is studied as a function of the porous diffusion coefficient, with the two limiting cases of slow and fast diffusion previously defined. To estimate the mean escape time of Mg-28 from the target, 10^6 events are simulated, ensuring a relative uncertainty on the average release time below 0.1%. In the simulation, each event corresponds to a generated and diffusing atom, with atoms uniformly distributed within the disk

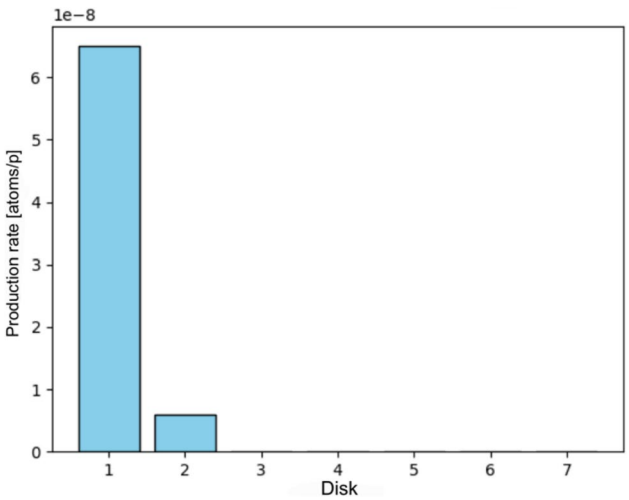

Fig. 5 Mg-28 production rate (atoms/proton) in the seven disks of the small target

volume. Initially, the release is simulated at a temperature of 1600 °C. Even considering the fast release model, the mean escape time is $(7.771 \pm 0.002) \cdot 10^4$ s for the small target and $(7.766 \pm 0.002) \cdot 10^4$ s for the big target. Both these values are comparable to the radionuclide half-life ($t_{1/2} \approx 20.9$ h), implying an important loss of isotopes due to decay before collection. As a matter of fact, assuming an average grain radius of $a = 7$ µm, one obtains from Eq. (2) a diffusion time of $\tau_{diff} \approx 21.1$ h.

Following the analysis of these results, the simulations can be used to suggest possible experimental improvements that would optimize radioisotope release. Hence, the temperature was increased in the next iteration of the simulations to 2000 °C and the grain size was reduced by one order of magnitude. Usually, the temperature limit for SiC, estimated as the highest temperature for which the observed mass loss stays below 0.5%, is fixed at 1800 °C. For higher temperature, the sample mass starts to decrease significantly, with a cumulative 4.2% mass loss at 2000 °C [28]. Assuming SiC targets capable of operating at 2000 °C with grain sizes one order of magnitude smaller, the predicted release times decrease from $(7.771 \pm 0.002) \cdot 10^4$ s to (9.961 ± 0.003) s for the small target and from $(7.766 \pm 0.002) \cdot 10^4$ s to (10.271 ± 0.003) s for the large target, corresponding to improvements by factors of 7802 and 7560, respectively. These predictions are independent of the porous diffusion model employed. Two mean diffusion time distribution plots using non-optimized and optimized parameters are reported in Fig. 6 considering the small target. Each target geometry shows nearly identical mean escape times from the two disks: the differences, ranging from 0.009% to 0.06% under every condition, are always lower or comparable to the statistical uncertainty of the simulation, quantified as 0.03%. The difference between slow and fast diffusion regimes is not significant within the statistical uncertainty, indicating that diffusion through grains is the dominant process governing the release.

A primary limitation of this study is the current unavailability of experimental measurements against which the simulation results could be validated, except for the part involving the LIS (see below), due to a discontinuous provision of proton beams at the SPES facility. Nevertheless, once SPES becomes fully operational and production-yield data for Mg-28 using RIBs are obtained, such data will provide an indispensable baseline for validating the theoretical model presented in this work and subsequently optimizing different target configurations across a wide range of operating temperatures.

Laser photo-ionization

The ionization efficiency is investigated by varying the average laser power between 10 µW and 10 W, corresponding to the highest order of magnitude achievable with the SPES online laser system [7]. The density matrix formalism is first used to analyze the saturation behavior of the resonant transitions. The saturation power of the first transition is defined as the minimum laser power required to equalize the populations of the ground and first excited states. Similarly, once the first transition is saturated, the saturation power of the second transition is defined as the minimum laser power needed to produce equal populations among the ground, first excited, and second excited states. In this work, populations are considered equal when their difference is within 0.5% at $T/2$. The saturation powers obtained are: $\bar{P}_1 = 220$ mW, $\bar{P}'_1 = 220$ mW, $\bar{P}_2 = 80$ mW, $\bar{P}'_2 = 280$ mW for the first transition of Scheme 1 and 2, and the second transition of

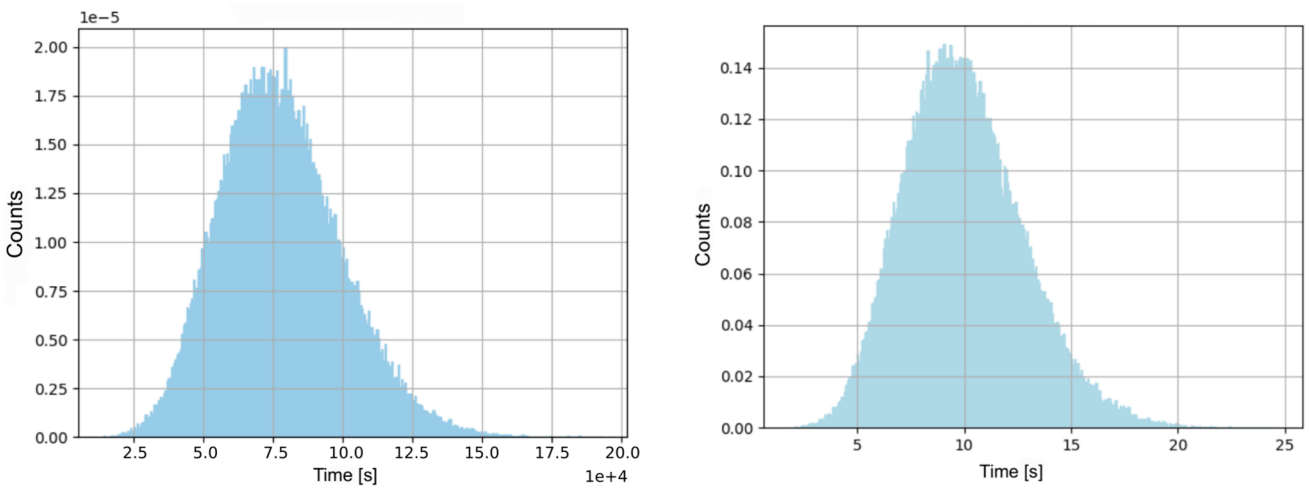

Fig. 6 Mean diffusion time distribution from disk 1 in the small target with non-optimized parameters (on the left) and optimized parameters (on the right) using the fast release model (D_p=10^{12} cm^2/s)

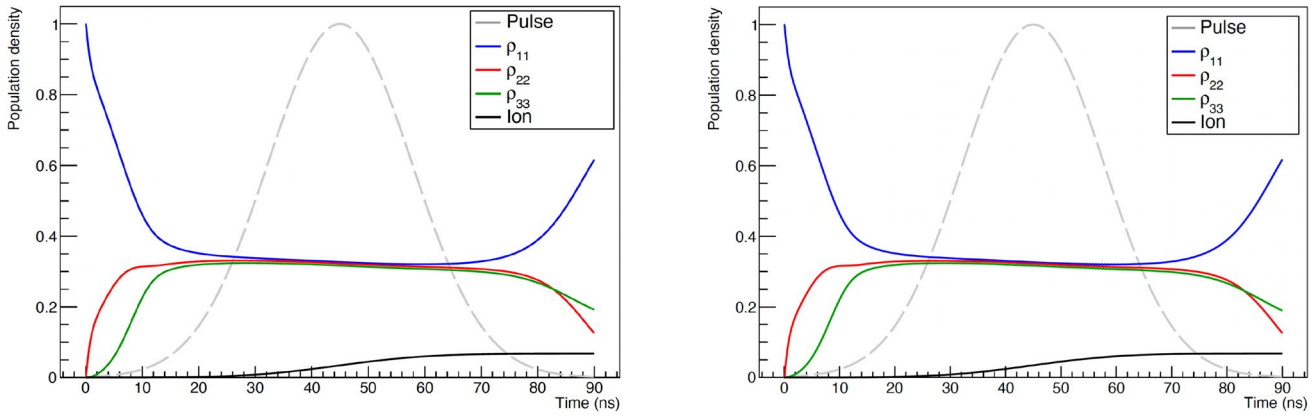

Fig. 7 Atomic population dynamics using two resonant lasers at saturation power and a third 30 W non-resonant laser. Scheme 1 on the left, Scheme 2 on the right

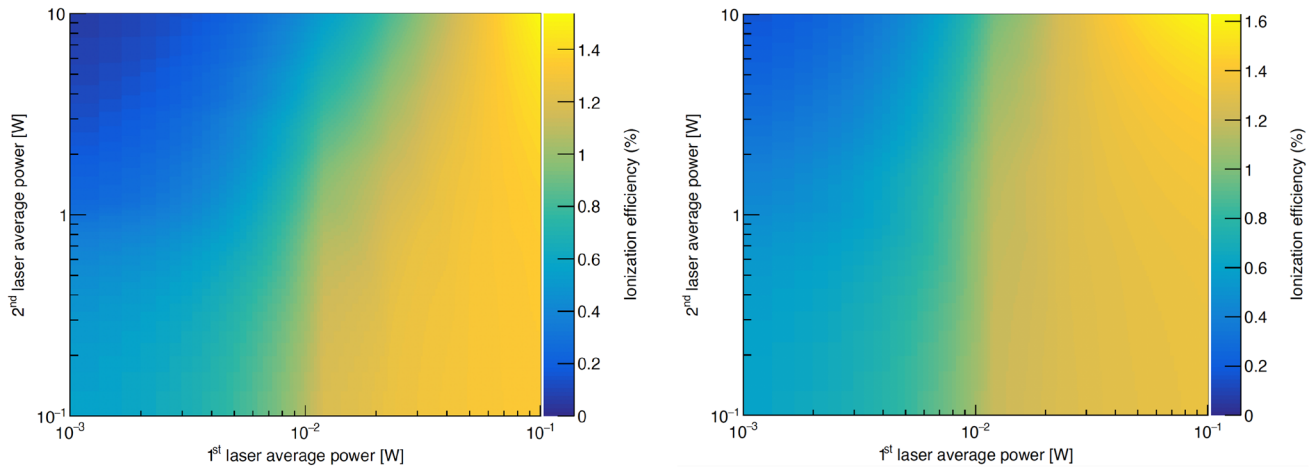

Fig. 8 Efficiency maps. Scheme 1 on the left, Scheme 2 on the right

Scheme 1 and 2 respectively. Population dynamics show that Scheme 2 requires significantly higher second-step power to reach saturation. For instance, using a 20 W green laser (532 nm), ion populations of 4.5% and 4.6% are achieved by the two schemes, respectively, with Scheme 2 appearing more efficient only because its second transition requires higher power to saturate and this slightly contributes to the non-resonant step. Increasing the power to 30 W raises the values to 6.7% in the first scheme and 6.8% in the second scheme, as shown in Fig. 7. At 40 W, the ion fraction further increases to 8.9% for both schemes. Applying the volume factor η mentioned before, it is possible to obtain the single-pulse ionization efficiency as a function of the average power of the two resonant lasers. The two schemes exhibit comparable efficiencies, with a maximum value of $\approx 1.2\%$, in the case of a 20 W non-resonant laser, $\approx 1.5\%$, in the case of a 30 W one and $\approx 1.8\%$, in the case of a 40 W one. The power maps of the efficiency using a 30 W non-resonant laser are shown in Fig. 8. The suitable power intervals for the resonant lasers are related to their wavelengths [7]. For both schemes, the efficiency is more sensitive to the power of the first resonant laser.

Table 4 Doppler FWHMs for each wavelength from Table 3

	Doppler FWHM (GHz)
λ_1	43
λ_2	14
λ_2'	22

Factors which could influence efficiency are the Doppler and the pressure broadening. The broadening of the Lorentzian profile due to these effects can be calculated for each transition [40] and the results for the Doppler broadening are summed up in Table 4.

Then, it is clear that using $\gamma_{Li} > 50$ GHz for both lasers would minimize the number of ions lost due to the Doppler effect. Regarding pressure broadening, starting from production rates in a SiC target calculated with FLUKA [38, 39] and following a procedure adopted in a previous study [23, 41], the total FWHM due to collisional effects is estimated to be lower than ≈ 2 MHz, which is negligible with respect to Doppler broadening.

Solving Eq. (17), it is possible to calculate the flux of ions exiting the ionization chamber and, eventually, the overall ionization efficiency as the ratio between the number of ions exiting the chamber and the number of atoms entering the chamber, calculated with Eq. (9). Looking at the plot shown in Fig. 9 it can be observed that the flux entering the ionization chamber becomes steady in times between 0 and 100 s only at high temperatures, namely at 2000 °C. Once the steady state in the transfer-line flux is achieved, the ion flux from the LIS becomes steady in a negligible time, as shown in Fig. 10.

The steady state of the ion flux is strongly influenced by the loss rate l, which is tunable with experimental data. Given that in a state-of-the-art ion source atoms survive around 10^{-3} s before being lost, then $l = 10^3$ s^{-1} [23]. Assuming a stable exiting flux and a single-pulse ionization efficiency of 1%, the overall ionization efficiency reaches 9.1% after five characteristic times. The overall efficiency can be evaluated for different resonant laser powers. When a non-resonant laser is also employed, the maximum efficiency is estimated to be approximately 11.0% at 20 W, 13.3% at 30 W, and 15.6% at 40 W. As an example, Fig. 11 shows the global efficiency map corresponding to a 30 W non-resonant laser.

ISOLDE measured the offline ionization efficiency of Mg in its Resonance Ionization Laser Ion Source (RILIS) using Scheme 2 and the following laser powers [6]: $\bar{P}_1 = 40$ mW, $\bar{P}_2 = 80$ mW, $\bar{P}_3 = 13{,}500$ mW, with $\tau_{FWHM} \leq 20$ ns for each laser. All the lasers were overlapped in time. The measured ionization efficiency is $\approx 10\%$. Performing the calculations with these parameters, the theoretical ionization efficiency is estimated to be $\approx 5.6\%$. This result is strongly dependent on the loss factor l: as a matter of fact, the measured value for efficiency can be found halving this factor, i.e., using $l = 0.5 \cdot 10^3$ s^{-1}, which is a realistic value. As l cannot be predicted, for the moment, by the simulation, a future perspective could be to implement its calculation starting from the existing literature [42] in order to improve efficiency estimations. In any case, the results are consistent with the measured values [6, 17, 43].

Considering the small target at a temperature of 2000 °C and fixing $l = 10^3$ s^{-1}, the collected activity of

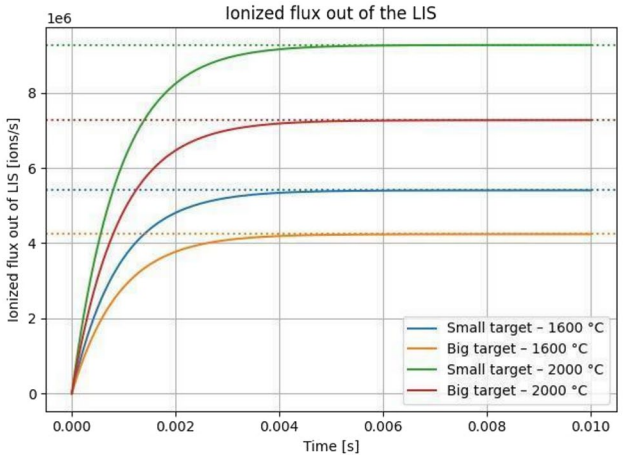

Fig. 10 Ionized flux exiting the LIS for small and big target at 1600 °C and 2000 °C

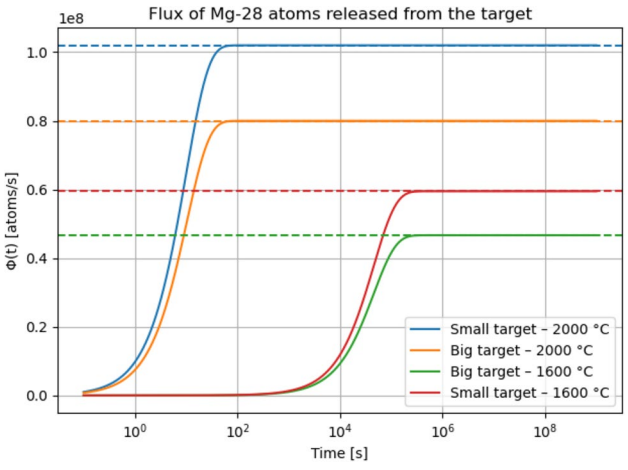

Fig. 9 Flux of Mg-28 atoms released from the target for the two conditions of target and temperature

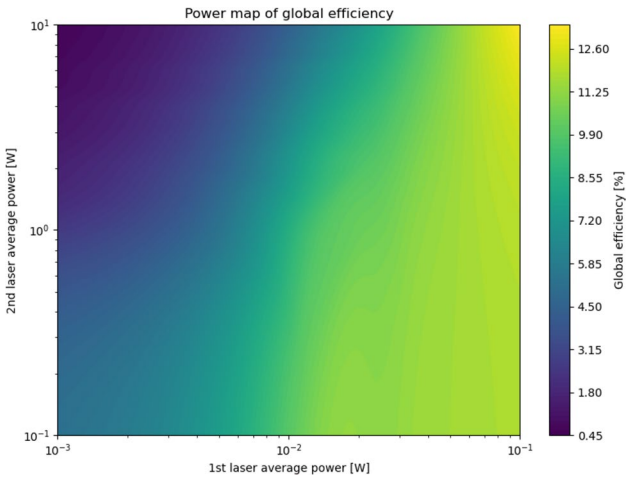

Fig. 11 Power map of global efficiency using a 30 W non-resonant laser

Mg-28 can be calculated using Eq. (21). For different laser configurations, we obtain the following values after one hour of irradiation:

- 20 W non-resonant laser: $A_{coll} \sim 0.35$ MBq;
- 30 W non-resonant laser: $A_{coll} \sim 0.43$ MBq;
- 40 W non-resonant laser: $A_{coll} \sim 0.51$ MBq.

Conclusions

Nuclei for innovative radiopharmaceuticals can be produced and studied exploiting the ISOL technique. In this study the production of Mg-28 at SPES, a radionuclide with important biological applications, has been analyzed for the optimization of production parameters. Simulations with GEANT4 allow to reproduce the experimental apparatus, a SiC target, and the processes occurring within it, namely diffusion and effusion. The production of Mg-28 is critically hindered by diffusion in grains, and, according to calculations, SiC targets with grain size one order of magnitude smaller and higher thermal resistance could produce Mg-28 with an efficiency very close to the unit. Furthermore, a new magnesium laser photo-ionization scheme reproducible at SPES was proposed and studied, obtaining a calculated overall ionization efficiency comparable to the one measured at CERN with another scheme ($\approx 10\%$).

In conclusion, a theoretical workflow for radioisotope production via the ISOL technique has been developed. Although direct experimental validation is currently missing, owing to the unavailability of the SPES facility, this work establishes a fundamental predictive baseline. Its first application to the case-study of Mg-28 suggested that this isotope could be produced only after certain improvements of the SiC targets currently used at SPES. Future developments will focus on the experimental validation of this framework upon SPES availability, its extension to other elements of interest, and the advanced modeling of loss rates within the ion source to refine ionization efficiency estimations.

Author contributions All authors contributed to the study conception and design. Material preparation, data collection and analysis were performed by G.S.V., S.L., L.Z. and A.Ar., under the supervision of E.M. and S.M. The first draft of the manuscript was written by G.S.V. and A.Ar. and all authors commented on previous versions of the manuscript. All authors read and approved the final manuscript.

Funding This work was carried out in the context of the SPES_MED experiment, funded by the INFN National Scientific Committee III (CSN3).

Data availability The simulated datasets can be made available upon request.

References

1. Nilsson T (2013) European RIB facilities – status and future. Nucl Instrum Methods Phys Res B 317:194–200. https://doi.org/10.1016/j.nimb.2013.06.037
2. Lindroos M, "Review of ISOL-type Radioactive Beam Facilities," in *Proceedings of the 9th European Particle Accelerator Conference (EPAC'04)*, Lucerne, Switzerland, July 2004, pp. 45–49
3. Andrighetto A, Centofante L, Gramegna F et al (2023) Low energy radioactive ion beams at SPES for nuclear physics and medical applications. Nucl Instrum Methods Phys Res B 541:236–239. https://doi.org/10.1016/j.nimb.2023.05.044
4. Lilli G (2023) Remote handling of radioactive targets at the SPES facility. Il Nuovo Cimento C 46:1–9. https://doi.org/10.1393/ncc/i2023-23032-y
5. Lassen J, Li R, Mostamand M et al (2023) Developments at TRIUMF's laser resonance ionization ion source & multi-element operation. Nucl Instrum Methods Phys Res B 541:137–140. https://doi.org/10.1016/j.nimb.2023.04.055
6. Marsh B (2013) Resonance Ionization Laser Ion. Sources. https://doi.org/10.5170/CERN-2013-007.203
7. Scarpa D, Mariotti E, Khwairakpam OS et al (2022) New solid state laser system for SPES: selective production of exotic species project at Laboratori Nazionali di Legnaro. Rev Sci Instrum 93:083001. https://doi.org/10.1063/5.0078913
8. Khwairakpam OS, Mancheva R, Au M et al (2024) The SPES laser ion source: time structure and laser enhancement measurements with Sm^+ beam. J Phys Conf Ser 2743:012066. https://doi.org/10.1088/1742-6596/2743/1/012066
9. Ogura T, Kobayashi NI, Suzuki H et al (2018) Magnesium uptake characteristics in *Arabidopsis* revealed by ^{28}Mg tracer studies. Planta 248:745–750
10. Watson WS, Hilditch TE, Horton PW et al (1979) Magnesium metabolism in blood and the whole body in man using ^{28}magnesium. Metabolism 28:90–95. https://doi.org/10.1016/0026-0495(79)90174-4
11. Kirchner R (1992) On the release and ionization efficiency of catcher-ion-source systems in isotope separation on-line. Nucl Instrum Methods Phys Res B Beam Interact Mater Atoms 70:186–199. https://doi.org/10.1016/0168-583X(92)95930-P
12. Santana-Leitner M (2005) A Monte Carlo code to optimize the production of radioactive ion beams by the ISOL technique. PhD, UPC-ETSEIB Catalunya TU
13. Egoriti L, Boeckx S, Ghys L et al (2016) Analytical model for release calculations in solid thin-foils ISOL targets. Nucl Instrum Methods Phys Res A 832:202–207. https://doi.org/10.1016/j.nima.2016.06.106
14. Zhang Y, Remec I, Alton GD, Liu Z (2010) Simulation of rare isotope release from ISOL target. Nucl Instrum Methods Phys Res A 620:142–146. https://doi.org/10.1016/j.nima.2010.04.015
15. Ballan M, Tosato M, Verona M et al (2020) Preliminary evaluation of the production of non-carrier added 111Ag as core of a therapeutic radiopharmaceutical in the framework of ISOLPHARM_Ag experiment. Appl Radiat Isot 164:109258. https://doi.org/10.1016/j.apradiso.2020.109258
16. Fink DA, Richter SD, Blaum K et al (2015) On-line implementation and first operation of the Laser Ion Source and Trap at ISOLDE/CERN. Nucl Instrum Methods Phys Res B Beam Interact Mater Atoms 344:83–95. https://doi.org/10.1016/j.nimb.2014.12.007

17. Overview - RIMS-Code. https://rims-code.github.io/schemes/mg/. Accessed 20 Apr 2026
18. Corradetti S, Biasetto L, Manzolaro M et al (2013) Neutron-rich isotope production using a uranium carbide - carbon nanotubes SPES target prototype. Eur Phys J A 49:56. https://doi.org/10.1140/epja/i2013-13056-1
19. Fujioka M, Arai Y (1981) Diffusion of radioisotopes from solids in the form of foils, fibers and particles. Nucl Instrum Methods Phys Res 186:409–412. https://doi.org/10.1016/0029-554X(81)90933-2
20. U. Köster (2000) *Ausbeuten und Spektroskopie radioaktiver Isotope bei LOHENGRIN und ISOLDE* (English title: *Yields and Spectroscopy of Radioactive Isotopes at LOHENGRIN and ISOLDE*), Ph.D. Thesis, Technische Universität München, Munich, Germany; CERN-THESIS-2001–002
21. Jost C (2010) Developments in target-ion source chemistry for ISOL facilities. Johannes Gutenberg-Universität Mainz
22. Haken H, Der Agobian R, Pauthier M (1965) Theory of laser cascades. Phys Rev 140:A437–A447. https://doi.org/10.1103/PhysRev.140.A437
23. Arzenton A, Mariotti E, Scarpa D et al (2025) Laser photo-ionization efficiency of 111Ag for medical use in the SPES-ISOLPHARM project. Appl Radiat Isot 226:112143. https://doi.org/10.1016/j.apradiso.2025.112143
24. Agostinelli S, Allison J, Amako K et al (2003) Geant4—a simulation toolkit. Nucl Instrum Methods Phys Res Sect A 506:250–303. https://doi.org/10.1016/S0168-9002(03)01368-8
25. Allison J, Amako K, Apostolakis J et al (2006) Geant4 developments and applications. IEEE Trans Nucl Sci 53:270–278. https://doi.org/10.1109/TNS.2006.869826
26. Allison J, Amako K, Apostolakis J et al (2016) Recent developments in Geant4. Nucl Instrum Methods Phys Res A 835:186–225. https://doi.org/10.1016/j.nima.2016.06.125
27. Andreetto P, Chiarello F, Costa F et al (2019) Merging OpenStack-based private clouds: the case of CloudVeneto.it. EPJ Web Conf 214:07010. https://doi.org/10.1051/epjconf/201921407010
28. Manzolaro M, Corradetti S, Ballan M et al (2021) Thermal and mechanical characterization of carbides for high temperature nuclear applications. Materials (Basel) 14:2689. https://doi.org/10.3390/ma14102689
29. Jiang W, Jung HJ, Kovarik L et al (2015) Magnesium behavior and structural defects in Mg+ ion implanted silicon carbide. J Nucl Mater 458:146–155. https://doi.org/10.1016/j.jnucmat.2014.12.071
30. Eichler B, Hübener S, Roßbach H (1985) Adsorption flüchtiger Metalle auf metallischen Oberflächen und Möglichkeiten ihrer Anwendung in der Kernchemie – Berechnung der Adsorptionsenthalpien der Actinoide. Zentralinstitut für Kernforschung Rossendorf, Rossendorf, Germany
31. Eichler B, Hübener S, Roßbach H (1985) Adsorption flüchtiger Metalle auf metallischen Oberflächen und Möglichkeiten ihrer Anwendung in der Kernchemie – Berechnung der Adsorptionsenthalpien der Seltenerdmetalle. Zentralinstitut für Kernforschung Rossendorf, Rossendorf, Germany
32. Roßbach H, Eichler B (1984) Adsorption von Metallen auf metallischen Oberflächen und Möglichkeiten ihrer Nutzung in der Kernchemie – Ermittlung von Adsorptionsenthalpien mit dem Rechenprogramm APO. Zentralinstitut für Kernforschung Rossendorf, Rossendorf, Germany
33. Pichard A, Jardin P, Saint-Laurent M-G et al (2010) Development of a surface ionization source for the SPIRAL 2 project. Rev Sci Instrum 81:02A908. https://doi.org/10.1063/1.3258498
34. Atomic spectral line database from CD-ROM 23 of R. L. Kurucz. https://lweb.cfa.harvard.edu/amp/ampdata/kurucz23/sekur.html. Accessed 17 Apr 2026
35. NIST: Atomic Spectra Database Lines Form. https://physics.nist.gov/PhysRefData/ASD/lines_form.html. Accessed 17 Apr 2026
36. Khwairakpam OS (2023) Study, Development and Optimization of Laser Resonant Photo-Ionization processes applied to species of interest for the Isolpharm-SPES project. PhD, University of Siena
37. Köster U (2002) Resonance ionization laser ion sources. Nucl Phys A 701:441–451. https://doi.org/10.1016/S0375-9474(01)01625-6
38. Home | The official CERN FLUKA website. https://fluka.cern/. Accessed 29 Apr 2026
39. Chen D (2026), *Development of ISOLPHARM Radionuclide Implantation Station (IRIS) in the Context of SPES-ISOLPHARM Project*, Ph.D. Thesis, University of Padova, Padova, Italy
40. Demtröder W (2008) Laser spectroscopy. Springer Berlin Heidelberg, Berlin
41. Mariotti L (2024) Studio della Dinamica dei Livelli Atomici dell'Argento-111 nell'Interazione con Radiazione Laser per il Progetto ISOLPHARM. University of Siena, Italy
42. Liu Y, Baktash C, Beene JR et al (2011) Time profiles of ions produced in a hot-cavity resonant ionization laser ion source. Nucl Instrum Methods Phys Res B 269:2771–2780. https://doi.org/10.1016/j.nimb.2011.08.009
43. Fedoseyev VN (1999) The use of lasers for the selective ionization of radionuclei for RIB generation. AIP Conference Proceedings. AIP, Denton, pp 296–300